

Model Predictive Thrust Force Control of a Linear Flux-Switching Permanent Magnet Machine with Voltage Vectors Selection and Synthesis

Wentao Huang, Wei Hua, Senior Member, IEEE, Fangbo Yin, Feng Yu, Member, IEEE, and Ji Qi

Abstract—To reduce the thrust force ripple of a complementary and modular linear flux-switching permanent magnet machine, a model predictive thrust force control (MPTFC) is developed and implemented based on the active voltage vectors selection (AVVS) and two-voltage-vector synthesis (TVVS). Firstly, the active VVs are screened and assigned to the specific sector, instead of traversing all the possible vectors, and consequently, significantly decrease prediction workload. Secondly, for the elimination of the weighting factor in the conventional MPTFC, the control object is transformed from the thrust force and stator flux to the stator flux only by using the load angle. Thirdly, to achieve the steady-state performance improvement, the TVVS approach is applied in each control period, where the optimal TVVS and its dwell time are simultaneously obtained by only one cost function. Both simulated and experimental results verify that the steady-state performance improvement can be realized by the developed MPTFC through comparing with normal hysteresis current control and conventional MPTFC strategies.

Index Terms— Linear, flux-switching permanent-magnet (FSPM) machine, model predictive control, duty cycle control, thrust force ripple, active voltage vectors selection.

I. INTRODUCTION

LINEAR flux-switching permanent magnet (PM) (LFSPM) machines have attracted increasing attention due to their simple and robust structure, higher power density, sinusoidal back EMF, and fault-tolerance capacity, as compared with other types of linear PM motors [1]. Hence, LFSPM machines have been widely researched for applications range from transportation systems to industrial application [2-3].

Manuscript received June 26, 2017; revised November 21, 2017, February 1, 2018, and March 18, 2018; accepted April 23, 2018. This work was supported in part by National Key R&D Program of China (2017YFB1300900) and the Fundamental Research Funds for Central Universities (2242016K41004).

Wentao Huang, Wei Hua, Fangbo Yin and Ji Qi are with the School of Electrical Engineering, Southeast University, Nanjing, 210096, China (e-mail: wentao.h@hotmail.com; huawei1978@seu.edu.cn; yinfbseu@sina.com; qj_1994@163.com).

Feng Yu is with the School of Electrical Engineering, Nantong University, Nantong, 226019, China (e-mail: yufeng628@ntu.edu.cn).

Due to the lack of additional teeth, the conventional LFSPM machines which are directly transformed from typical rotary FSPM machines, will suffer from the disadvantages of asymmetrical magnetic circuit in the end coil and unfavorably large cogging force. To address these problems, complementary and modular LFSPM (CMLFSPM) machines have been proposed and investigated in [4]. The structures of the non-complementary modular LFSPM (MLFSPM) machine and the CMLFSPM machine are illustrated in Fig. 1. As shown in Fig. 1(b), the relative displacements between the two E-shaped modules of one phase in the CMLFSPM machine are mutually 180 electrical degrees apart. Hence, it can offer sinusoidal back electromotive force, and smaller cogging force and thrust force ripples [5].

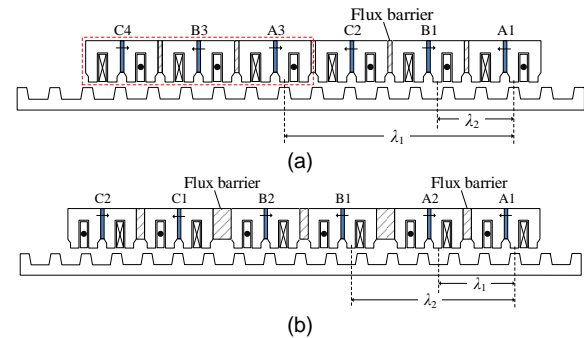


Fig. 1. Cross section of MLFSPM machines. (a) Non-complementary structure. (b) Complementary structure.

The recent researches on CMLFSPM machines mainly concentrate on the structure, operation principle, mathematical model, and static thrust force performance. Few attentions are paid to the high-performance control. Very recently, based on the theory of the mover flux-oriented control, a closed-loop speed control strategy has been applied for the CMLFSPM machine, and the conclusions indicate that the conventional field-oriented control (FOC) strategy can be implemented in the CMLFSPM machines [6]. However, the thrust force has not been studied, and the switching pulse is actually generated by hysteresis current control (HCC), which results in irregular switching frequency and relatively large thrust force ripple. Hence, in order to further reduce the thrust force ripple and realize high-performance control of the CMLFSPM machines, model predictive control (MPC) strategy is investigated and developed in this paper.

MPC has been researched in conjunction with rotary FSPM machine drives recently [7-9]. According to the control variables, MPC strategies can mainly be categorized into two types, namely, model predictive current control (MPCC) [10-11] and model predictive torque control (MPTC) [12-14]. MPCC is normally selected in the manner where stator armature currents are considered specifically to produce less total harmonic distortion (THD) when compared with conventional HCC. Evolving from direct torque control (DTC), MPTC is proposed with the focus on optimizations of both torque and stator flux magnitudes.

To achieve satisfactory steady-state performance of voltage-source-inverter (VSI)-fed machine drives, sampling frequency of conventional MPTC has to be high, which inevitably imposes a heavy computational burden on practical implementation. Although MPTC is more flexible and effective than DTC in voltage vector (VV) determination, applying the selected VV during the entire control period is not optimal in terms of torque ripple reduction [15]. In order to improve steady-state performance, the method of calculating the proper VV is researched in conjunction with the duty cycle control (DCC) [16-19]. In [17], a generalized two-vector-based MPTC approach is proposed in a manner where two arbitrary VVs are optimized and used in each control period. For the alleviation of computational cost, the number of possible VV combinations have decreased from 49 to 25. In order to reduce torque and flux ripples, an improved two-vector-based duty cycle optimization is introduced in [18], where the selected VVs can be two nonzero vectors and their durations are calculated based on flux error minimization only. Inheriting the merits of the proper VV calculation and DCC, this paper develops a model predictive thrust force control (MPTFC) strategy based on active VV selection (AVVS) and two-voltage-vector synthesis (TVVS) for thrust force ripple reduction of the CMLFSPM machines.

The arrangement of the paper is organized as followed. Section II describes the structure and mathematic model of the CMLFSPM machine. In Section III, a conventional MPTFC algorithm is deduced firstly. Then, in Section IV a developed MPTFC strategy based on AVVS and TVVS is proposed. Consequently, the performance of the CMLFSPM machine under the developed scheme is analyzed by simulations and experimental verifications in Section V and Section VI, respectively. Finally, conclusions are drawn in Section VII.

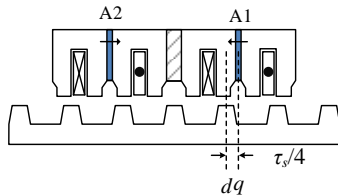


Fig. 2. Definition of dq -axes for the LFSPM machine.

II. MATHEMATIC MODEL OF THE CMLFSPM MACHINE

A. Definition of dq -Axes

The dq -axes of the CMLFSPM machine is defined in Fig. 2. The q -axis is the primary position where the value of PM flux linkage is zero, and the d -axis is the primary position where the PM flux linkage reaches the maximum value. The relative

displacement between d - and q -axis is $\tau_s/4$, where τ_s is the stator pole pitch.

B. Mathematic Model

Based on the definition above, the dq -axes inductances are

$$\begin{cases} L_d=L_{DC}+L_m \cos(3\theta_e)/2 \\ L_q=L_{DC}-L_m \cos(3\theta_e)/2 \\ L_{dq}=L_{qd}=L_m \sin(3\theta_e)/2=0 \end{cases} \quad (1)$$

where, θ_e is electrical degree of the primary position; L_{DC} and L_m are the DC component and amplitude of the fundamental component of self-inductance, respectively. However, since L_m is so small, it is neglected in this paper, which means $L_d=L_q=L_{DC}=L_s$, and L_s is the average stator armature inductance.

The differential equations of dq -axes currents and voltages can be written as

$$\begin{cases} \frac{di_d}{dt}=-R_s i_d/L_s+\omega_e i_q+u_d/L_s \\ \frac{di_q}{dt}=-\omega_e i_d-R_s i_q/L_s+(u_q-\omega_e \psi_f)/L_s \end{cases} \quad (2)$$

$$\begin{cases} u_d=\frac{d\psi_{sd}}{dt}-\omega_e \psi_{sq}+R_s i_d \\ u_q=\frac{d\psi_{sq}}{dt}+\omega_e \psi_{sd}+R_s i_q \end{cases} \quad (3)$$

where, i_d/i_q , u_d/u_q and ψ_{sd}/ψ_{sq} are the dq -axes currents, voltages and stator flux linkages, respectively; R_s is phase resistance; $\omega_e=2\pi v/\tau_s$ is the electrical angular velocity; v is the mover speed.

Neglecting L_m , the stator flux linkage in the dq -axes can be defined as

$$\begin{cases} \psi_{sd}=L_s i_d+\psi_f \\ \psi_{sq}=L_s i_q \end{cases} \quad (4)$$

where, ψ_f is the amplitude of three-phase PM flux linkages in stationary reference frame, i.e., d -axis PM flux linkage.

According to (4), electromagnetic thrust force is deduced as

$$\begin{aligned} F_e &= 3/2[(d\psi_{sd}/dt-\omega_e \psi_{sq})i_d+(d\psi_{sq}/dt+\omega_e \psi_{sd})i_q]/v \\ &= 3\pi \psi_f i_q / \tau_s \end{aligned} \quad (5)$$

Due to the similar dq -axes inductances of the CMLFSPM machine, $i_d=0$ control, equivalent to maximum torque per ampere control, is employed to minimize stator copper loss.

The dynamic equation of the mover can be expressed as

$$F_e=(m+m_L)p v + F_D + F_C + F_L \quad (6)$$

where, m and m_L are the mass of the mover and load, respectively; p is the differential operator; F_D is viscous friction force; F_C is the Coulomb friction; and F_L is load force.

III. CONVENTIONAL MODEL PREDICTIVE THRUST FORCE CONTROL OF THE CMLFSPM MACHINE

Based on the conventional MPTC of rotary FSPM machines, the electromagnetic thrust force and the magnitude of stator flux linkage are selected as the control objects in the conventional MPTFC method for the CMLFSPM machine.

A. Predictive Model

Applying the Euler formula to discretize the CMLFSPM machine mathematic model and transforming the result into a

single time step, the predictive current, predictive stator flux linkage, and predictive thrust force models are derived as

$$\begin{cases} i_d(k+1) = (1 - R_s T_s / L_s) i_d(k) + T_s \omega_e i_q(k) + T_s u_{id}(k) / L_s \\ i_q(k+1) = -T_s \omega_e i_d(k) + (1 - R_s T_s / L_s) i_q(k) + T_s [u_{iq}(k) - \omega_e \psi_s] / L_s \end{cases} \quad (7)$$

$$\begin{cases} \psi_{sd}(k+1) = L_s i_d(k+1) + \psi_s \\ \psi_{sq}(k+1) = L_s i_q(k+1) \end{cases} \quad (8)$$

$$\psi_s(k+1) = \sqrt{\psi_{sd}^2(k+1) + \psi_{sq}^2(k+1)} \quad (9)$$

$$F_e(k+1) = 3\pi \psi_s i_q(k+1) / \tau_s \quad (10)$$

where, k and $(k+1)$ means the current and next sampling step, respectively; T_s is sample time; u_{id}/u_{iq} are the basic VVs in dq -axes.

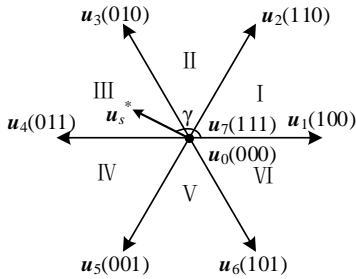


Fig. 3. Basic 8 VVs and 6 sectors for a two-level VSI-fed drive.

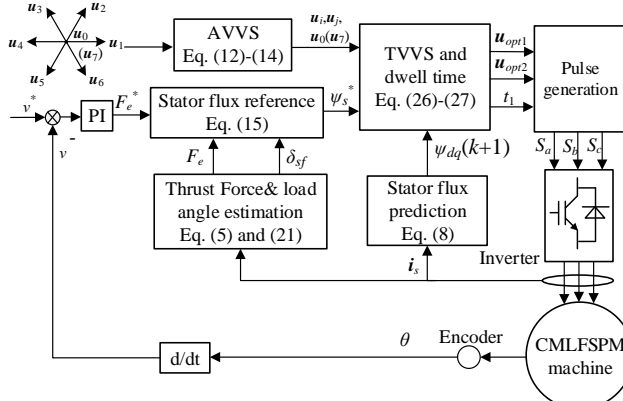


Fig. 4. Control diagram of the developed MPTFC strategy.

B. Cost Function

In order to obtain the optimal VVs, a cost function is designed in a manner where the absolute errors between the referenced and predicted values are adopted as follows

$$g_i = |F_e^* - F_e(k+1)| + \lambda |\psi_s^* - \psi_s(k+1)| \quad (11)$$

where, F_e^* and ψ_s^* are the referenced thrust force and stator flux. λ is a weighting factor to connect the above two variables with different dimensions.

For a two-level VSI-fed three-phase CMLFSPM machine, there are eight ($i=8$) basic VVs (six nonzero VVs, and two zero VVs), as shown in Fig. 3.

When the conventional MPTFC method is applied, the optimal VV which minimizes the cost function is employed and used during the entire control period. It should be noted that the selection process of the optimal VV including the traversals of all basic VVs, which will impose a high computational burden on the controller. Besides, the single optimal VV will result in relatively large thrust force ripple, flux ripple and high THD of

phase currents. To overcome the drawbacks above, a new MPTFC strategy based on active VVs selection (AVVS) and two-voltage-vector synthesis (TVVS) is developed for the CMLFSPM machine. The load angle will be employed to transform the control variable from the thrust force and stator flux to the stator flux only, eliminating the weighting factor in the cost function. Besides, the active VVs selection is designed to decrease the number of VV candidates for cost function optimization, resulting in the reduction of computational burden. To enhance steady-state performance, two-voltage-vector synthesis will be applied in each control period rather than single VV to minimize tracking errors.

IV. NEW MODEL PREDICTIVE THRUST FORCE CONTROL

The control diagram of the new MPTFC strategy is shown in Fig. 4. In the developed control scheme, first, the deadbeat control concept is used to select appropriate active VVs precisely, and the load angle is calculated to establish the relationship between the thrust force and stator flux. Then, two VVs from the selected VVs are synthesized as candidate VVs. Finally, the optimal TVVS and its dwell time are determined by optimizing the cost function. The detailed information of the control diagram will be elaborately introduced as follows.

A. Active Voltage Vector Selection (AVVS)

From the basic VVs, considering the two zero vectors as the same vector, 49 (7×7) TVVSs can be obtained [17]. Especially, if the two VVs in a TVVS are the same, the selected TVVS is the identical in the effect with the single VV. Yet, the syntheses process of 49 VVs will bring tremendous burden during the real-time implementation, hence, it is necessary to reduce the traversals of TVVSs.

Based on the deadbeat solution in [20], the candidates of VVs can be assigned to a specific sector by calculating the VV reference. The amplitude of the stator flux can be estimated by the stator flux linkage equation in (4). Accordingly, the angle of the stator flux vector θ_s can be calculated as

$$\theta_s = \arctan(\psi_{s\beta}^* / \psi_{sa}^*) \quad (12)$$

Adopting the load angle δ_{sf} , which is the angle between the stator flux vector and PM flux vector, both the amplitude and angle of the VV reference in the $a\beta$ -axes can be expressed as

$$\begin{cases} u_{sa}^* = [\psi_{sa}^* \cos(\theta_s + \Delta\delta_{sf}) - \psi_{sa}] / T_s + R_s i_{sa} \\ u_{s\beta}^* = [\psi_{s\beta}^* \sin(\theta_s + \Delta\delta_{sf}) - \psi_{s\beta}] / T_s + R_s i_{s\beta} \end{cases} \quad (13)$$

$$\gamma = \arctan(u_{s\beta}^* / u_{sa}^*) \quad (14)$$

where, $\psi_{sa}^*/\psi_{s\beta}^*$ are the stator flux references in $a\beta$ -axes, and $\Delta\delta_{sf}$ is the load angle deviation.

TABLE I
CLASSIFICATION OF VOLTAGE VECTORS

Group	Sector	Active voltage vectors
1	I	$u_1, u_2, u_0(u_7)$
2	II	$u_2, u_3, u_0(u_7)$
3	III	$u_3, u_4, u_0(u_7)$
4	IV	$u_4, u_5, u_0(u_7)$
5	V	$u_5, u_6, u_0(u_7)$
6	VI	$u_6, u_1, u_0(u_7)$

From equation (14), it can be found that the angle position can locate the objective sector as well as the active VVs. According the definition of sectors, the syntheses of 49 VVs

can be classified into six groups, and each group can determine 9 (3×3) candidates of TVVSs, as listed in Table I. For example, as shown in Fig. 5(a), the VV reference is located in Sector III, and \mathbf{u}_3 , \mathbf{u}_4 and $\mathbf{u}_0(\mathbf{u}_7)$ should be the active VVs according to Table I. Referring the theory of space vector modulation, the optimal TVVS can be generated from the selected active VVs.

On the basis of the stator flux adaptive approach and $i_d=0$ control [14], the amplitude of the stator flux reference is calculated as

$$\psi_s^* = \sqrt{\psi_f^2 + [\tau_s F_e L_s / (3\pi\psi_f)]^2} \quad (15)$$

Neglecting the reluctance thrust force and substituting the load angle δ_{sf} into (5), the expression of thrust force can be rewritten as

$$F_e = 3\pi\psi_f\psi_s \sin\delta_{sf}/(\tau_s L_s) \quad (16)$$

The following equation is obtained by differentiating (16)

$$\frac{dF_e}{dt} = 3\pi\psi_f\psi_s \cos\delta_{sf}/(\tau_s L_s) \frac{d\delta_{sf}}{dt} \quad (17)$$

Equation (17) can be rewritten as

$$\Delta F_e = 3\pi\psi_f\psi_s \cos\delta_{sf} \Delta\delta_{sf}/(\tau_s L_s) \quad (18)$$

where, ΔF_e and $\Delta\delta_{sf}$ are the errors of thrust force and load angle between references and k th samples, respectively. The thrust force reference can be obtained through the speed regulator, and thrust force at k th sample can be calculated using equation (5).

In (18), if the amplitude of the stator flux ψ_s is constant, the load angle deviation $\Delta\delta_{sf}$ will determine the thrust force deviation ΔF_e , which means the control of the thrust force can be transformed to the control of the load angle. Hence, the load angle deviation can be derived as

$$\Delta\delta_{sf} = \tau_s L_s \Delta F_e / (3\pi\psi_f\psi_s \cos\delta_{sf}) \quad (19)$$

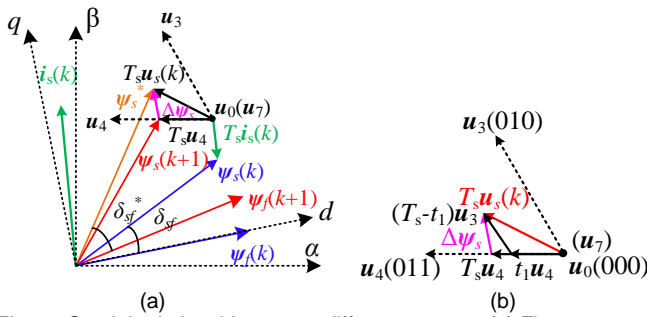


Fig. 5. Spatial relationship among different vectors. (a) Flux vectors of stator and mover in different reference frames. (b) VVs in Sector III.

B. Thrust Force Estimation and Stator Flux Reference Calculation

The thrust force can be estimated based on (5). According to the definition of the load angle, the current and referenced load angle are obtained as equations (20) and (21), respectively

$$\delta_{sf} = \theta_s - \theta_r = \arctan(\psi_{s\beta}/\psi_{sa}) - \theta_r \quad (20)$$

$$\delta_{sf}^* = \delta_{sf} + \Delta\delta_{sf} = \arctan(\psi_{s\beta}/\psi_{sa}) - \theta_r + \tau_s L_s \Delta F_e / (3\pi\psi_f\psi_s \cos\delta_{sf}) \quad (21)$$

where, θ_r is the angle of the PM flux vector due to the mover.

Based on the model predictive flux control strategy proposed in [14], the stator flux references in dq -axes can be obtained by using only the references of stator flux amplitude and load angle

$$\begin{cases} \psi_{sd}^* = \psi_s^* \cos\delta_{sf}^* \\ \psi_{sq}^* = \psi_s^* \sin\delta_{sf}^* \end{cases} \quad (22)$$

Combining (18), (21) and (22), it can be found that the control object has been transformed to the stator flux from the thrust force and stator flux. Fortunately, the cost function can be designed only to consider the limitation on the stator flux, and the weighting factor can be eliminated.

C. Stator Flux Prediction

Different from the conventional MPTFC method, the developed strategy applies a TVVS which includes two VVs in each control period. Therefore, the predictive current model is newly designed as follows

$$\begin{cases} i_d(k+1) = (1-R_s T_s L_s) i_d(k) + T_s \omega_e i_q(k) + t_1 u_{id}(k) / L_s \\ \quad + (T_s - t_1) u_{jd} / L_s \\ i_q(k+1) = -T_s \omega_e i_d(k) + (1-R_s T_s / L_s) i_q(k) + t_1 u_{iq}(k) / L_s \\ \quad + (T_s - t_1) u_{jq} / L_s - T_s \omega_e(k) \psi_f / L_s \end{cases} \quad (23)$$

where, u_{id}/u_{iq} and u_{jd}/u_{jq} are the first and second active VVs, obtained from the AVVS algorithms; t_1 is the dwell time of the first active VV, and $i=\{1,2,3\}$, $j=\{1,2,3\}$.

For the stator flux prediction, the predictive model is consistent with that of the conventional MPTFC method. It should be noted that the thrust force prediction is not required due to the employment of load angle.

D. Optimal Voltage Vector Synthesis and Dwell Time Calculation

As shown in Fig. 5(a), the error of stator flux vector $\Delta\psi_s$ establishes the relation between the stator flux and the VV reference \mathbf{u}_s is as follows [23]:

$$\Delta\psi_s = \psi_s^* - \psi_s(k+1) = T_s \mathbf{u}_s \quad (24)$$

According to the volt-second balancing principle [24], which is illustrated in Fig. 5(b), the dwell time of the VVs can be expressed as

$$T_s \mathbf{u}_s = t_1 \mathbf{u}_i + (T_s - t_1) \mathbf{u}_j \quad (25)$$

From (25), the dwell time of the first VV can be deduced as:

$$t_1 = \frac{(\mathbf{u}_s - \mathbf{u}_j) \cdot (\mathbf{u}_i - \mathbf{u}_j)}{|\mathbf{u}_i - \mathbf{u}_j|^2} T_s \quad (26)$$

Substituting (26) into (23), the current prediction can be obtained under different VV syntheses.

Consequently, a cost function including only the reference and prediction of the stator flux is constructed to select the optimal TVVS as follows:

$$c = |\psi_{sd}^* - \psi_{sd}(k+1)| + |\psi_{sq}^* - \psi_{sq}(k+1)| \quad (27)$$

E. Switching Pulse Generation

Upon the optimal TVVS and its dwell time are obtained, the relevant switching pulses for the next control period can be generated based on the DCC technique. To reduce the switching power losses of the VSI, two zero vectors (\mathbf{u}_0 and \mathbf{u}_7) should be selected appropriately, e.g., the vectors $\mathbf{u}_1(100)$, $\mathbf{u}_3(010)$ and $\mathbf{u}_5(001)$ should be followed by $\mathbf{u}_0(000)$, while the other vectors should be followed by $\mathbf{u}_7(111)$ [21]. For example, in Sector IV, if $\mathbf{u}_4(011)$ and a zero vector are selected as the optimal TVVS, the zero vector must be $\mathbf{u}_7(111)$ instead of $\mathbf{u}_0(000)$.

Summarily, the developed MPTFC can be implemented in the following steps:

- 1) Measure the stator current, mover position and DC-link voltage.
- 2) Calculate the VV reference based on the measured values.
- 3) Select the active VVs.
- 4) Estimate the thrust force and load angle at the current control period.
- 5) Calculate the stator flux reference.
- 6) Establish the predictive model and predict the stator flux.
- 7) Design and optimize the cost function for the optimal TVVS and dwell time.
- 8) Generate the switching pulses based on the optimal TVVS.

F. Comparisons with Existing MPC Methods

When comparing with the two-vector-based MPC in [17], the VVs in the developed MPC have been screened and limited in one specific sector by calculating the objective VV. During the process of cost function minimization, the active VV combinations have been reduced to 9 in this study, which is nearly one third of that in [17]. Hence, the developed MPTFC method can decrease the computational burden in practical implementations.

Although being similar with the improved MPC scheme in [18], the control objects have been changed from the thrust force and stator flux to the stator flux only in this paper, and consequently avoided the determination process of the weighting factor. However, it should be emphasized that two arbitrary VVs are selected by two cost function optimizations separately in [18]. In this paper, the two VVs of the optimal TVVS are determined by only one cost function simultaneously. Furthermore, due to the use of AVVS, the number of the active VV combinations in the developed MPC is half of that in [18]. Hence, the developed MPC strategy can reduce both the prediction workload and the algorithm complexity.

TABLE II

PARAMETERS AND SPECIFICATIONS OF THE CMLFSPM MACHINE

Items	Specifications
Stator pole pitch, τ_s (mm)	36
Phase resistance, R_s (Ω)	1.5
D-axis inductance, L_d (mH)	26.085
Q-axis inductance, L_q (mH)	26.255
PM flux-linkage, ψ_f (Wb)	0.216
Rated power, P_N (W)	1000
Rated speed, v_N (m/s)	1.5
Rated thrust force, F_e (N)	711
Rated current in RMS value, I_{rms} (A)	6

V. SIMULATION VERIFICATIONS

To investigate the effectiveness of the developed MPTFC on the CMLFSPM machine (the parameters and specifications are listed in Table II), simulations are conducted in the environment of MATLAB/Simulink. The performance of the CMLFSPM machine under HCC [6], conventional MPTFC and the developed MPTFC are compared and evaluated in detail. The identical PI controller ($K_P=500$, and $K_I=10000$) are adopted to regulate the speed loop in three control strategies. The hysteresis width in the HCC is ± 0.05 A, and $\lambda=2000$ is selected as the optimal weighting factor for the conventional MPTFC.

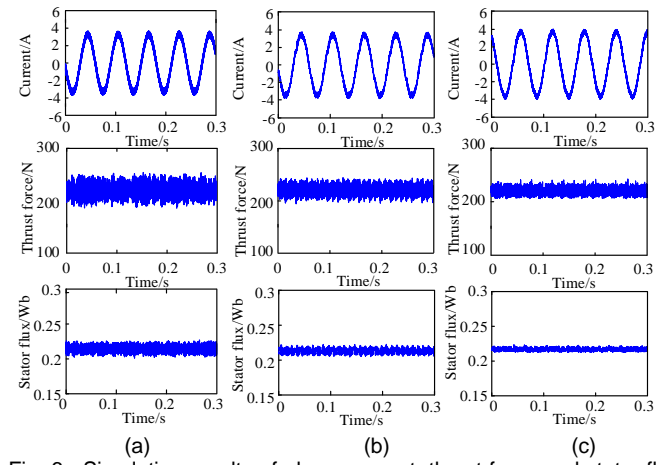


Fig. 6. Simulation results of phase current, thrust force and stator flux linkage at 0.6m/s without external load force by (a) HCC, (b) conventional MPTFC, and (c) the developed MPTFC.

TABLE III
SIMULATED STEADY-STATE PERFORMANCE UNDER THREE METHODS

Methods	Current THD (%)	Force ripple (%)	Flux ripple (%)
HCC	9.32	5.32	2.15
Conventional MPTFC	7.53	3.93	1.26
Developed MPTFC	4.36	2.53	0.8

Fig. 6 shows the simulated steady-state performances of the CMLFSPM machine under HCC, the conventional MPTFC and the developed MPTFC at the speed reference of 0.6m/s without external load force. It should be noted that the viscous friction force F_D and Coulomb friction force F_C are influenced by the manufacturing level of the linear guide and the mover. According to the experimental results, $F_D=120$ N and $F_C=100$ N are specified in the simulations. It can be found from Figs. 6(a) and 6(b), the thrust force and stator flux ripples have reduced under the conventional MPTFC due to the limitation on the thrust force and the stator flux linkage.

As shown in Fig. 6(c), the thrust force and flux ripples have been further suppressed under the developed MPTFC strategy. The reason is that the using of TVVS can reduce control errors, thus decreasing thrust force and flux ripples. The simulated results of the steady-state performance by three control methods in terms of phase armature current THD, percent force ripple F_{rip} and flux ripple ψ_{rip} are summarized in Table III. The definition of phase current THD, the percent force ripple and flux ripple are given by the following equations (28)-(30) [22],

$$\text{THD} = \sqrt{\sum_{n=2}^{\infty} I_n^2 / I_1^2} \times 100\% \quad (28)$$

$$F_{rip} = \sqrt{\frac{1}{N} \sum_{i=1}^N (F_e(i) - F_{AVE})^2 / F_{AVE}} \times 100\% \quad (29)$$

$$\psi_{rip} = \sqrt{\frac{1}{N} \sum_{i=1}^N (\psi_s(i) - \psi_{AVE})^2 / \psi_{AVE}} \times 100\% \quad (30)$$

where, I_n is the amplitude of n -order harmonic components, and I_1 is the amplitude of fundamental component; F_{AVE} and ψ_{AVE} are the average values of the thrust force and stator flux linkage; $F_e(i)$ and $\psi_s(i)$ are the instantaneous values of thrust force and stator flux linkage; and N is the number of samples.

The simulated steady-state results verify that the developed MPTFC for the CMLFSPM machine can decrease the current THD, thrust force ripple and stator flux ripple significantly.

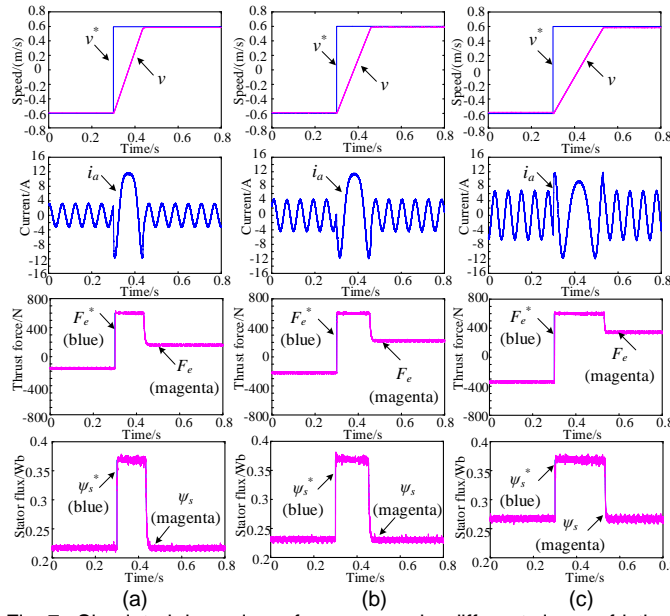


Fig. 7. Simulated dynamic performance under different viscous friction coefficient B by the developed MPTFC. (a) $B=100\text{Ns/m}$. (b) $B=200\text{Ns/m}$. (c) $B=400\text{Ns/m}$.

The influences of parameter variations of the CMLFSPM machine have been investigated in this research for a comprehensive evaluation of the developed MPTFC method.

As mentioned in [6], the viscous friction F_D is expressed as

$$F_D = Bv \quad (31)$$

where, v is the speed. B is the viscous friction coefficient, which is determined by the manufacturing quality of linear guide and machining error, and barely changed during the real implementation. Hence, a simulation is carried out to investigate its impact on the dynamic speed response. Fig. 7 presents the simulated speed reversal (-0.6m/s to 0.6m/s) under different values of B (100Ns/m, 200Ns/m and 400Ns/m), where 200Ns/m is the actual viscous friction coefficient of the linear machine drive. The speed settling times in Fig. 7(a), Fig. 7(b) and Fig. 7(c) are 0.14s, 0.17s and 0.24s, respectively. Obviously, a larger viscous friction coefficient B will certainly increase the viscous friction force, resulting in an increment of the speed response time. Moreover, as the thrust force increases, the amplitude of the stator flux rises accordingly due to the adaption of the stator flux adaptive approach, which agrees well with theoretical analysis. It is worth noting that the simulation results for the actual viscous friction coefficient can be validated by the experimental results, as shown in Fig. 12(c).

VI. EXPERIMENTAL VERIFICATIONS

In this section, experiments are conducted on a three-phase prototyped CMLFSPM machine with the same parameters listed in Table II. The experiment setup is shown in Fig. 8. The actual mover position is obtained by a linear encoder. The phase currents and DC-link voltage are measured by LEM HAS 50-S current sensor and LEM LV25-P voltage transducer, respectively. The control algorithm is implemented in a

dSPACE-1104 controller, and 8kHz is selected as the sampling frequency, which is determined based on the performance of the core of the dSPACE-1104 controller.

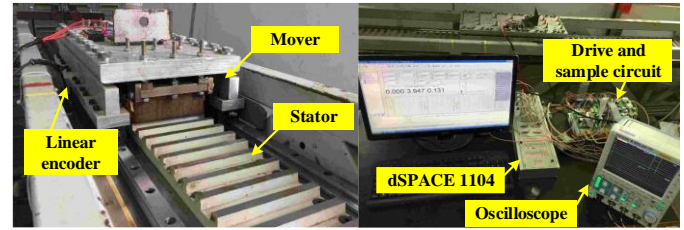


Fig. 8. Prototype of the CMLFSPM machine and experiment setup.

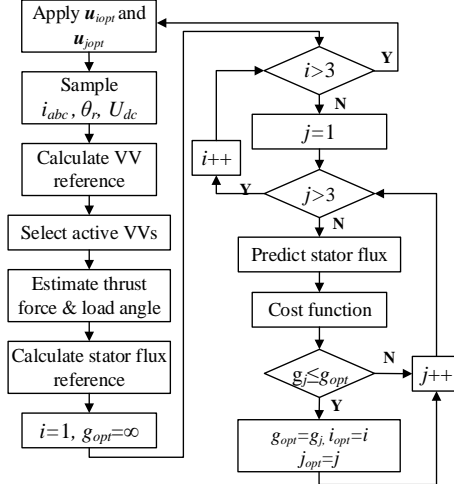


Fig. 9. Flow diagram of the developed MPTFC method.

Fig. 9 illustrates the flow diagram of the developed MPTFC scheme. The control strategy is implemented in MATLAB/Simulink combined with the real-time interface (RTI) of the DS1104 board which is a complete real-time control system based on a 603 PowerPC floating-point processor running at 250MHz. It is worth noting that the core code of the developed control algorithm is programmed in the embedded MATLAB function. All signals of the developed control strategy can be accessed, and control commands can be inputted by using ControlDesk online [25].

For the implementation of the digital control scheme, the microprocessor needs time to execute the algorithm, where it takes one sampling cycle to obtain the optimal TVVS. In order to achieve the exact prediction of the stator flux, the system computation delay should be taken into account. Hence, the delay compensation is applied as proposed in [26].

A. Steady-state Performance

Firstly, the steady-state performance of the CMLFSPM machine under HCC, the conventional MPTFC and developed MPTFC are compared in Fig. 10, where the speed controller parameters are kept the same ($K_p=800$ and $K_i=8000$) and the sampling interval for speed control loop is set to 8kHz. The hysteresis width is the same with that of simulations, and $\lambda=3000$ is selected as the optimal weighting factor for the conventional MPTFC during the implementation.

As shown in Fig. 10, it can be found that all the speed waveforms are stable and the phase current waveforms are sinusoidal. In addition, both the conventional and the developed MPTFC methods can reduce the force and flux

ripples compared to HCC method. From Table IV, the thrust force ripples are 8.76%, 6.82% and 3.56% with respect to HCC, the conventional and the developed MPTFC, meanwhile the flux ripples are 2.46%, 2.13% and 1.56%, respectively.

The experimental steady-state results prove that the developed MPTFC can significantly improve the current performance and reduce both thrust force and stator flux ripples.

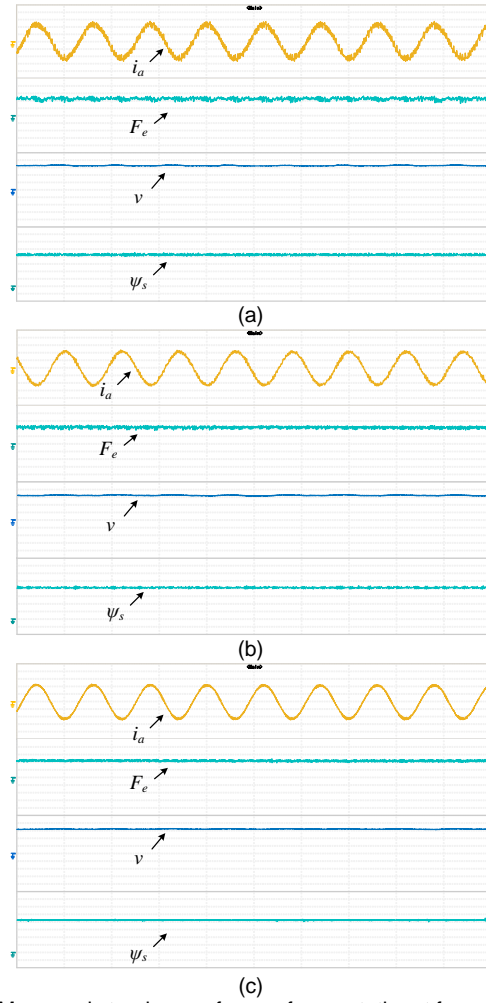


Fig. 10. Measured steady waveforms of current, thrust force, stator flux and speed at 0.6m/s by (a) HCC, (b) conventional MPTFC and (c) the developed MPTFC. (Current (2A/div), thrust force (100N/div), speed (0.2m/s/div), stator flux (0.05Wb/div), time (50ms/div))

In addition, the tracking errors of the thrust force have been calculated to further validate the tracking ability of the developed MPTFC strategy. Fig. 11 shows the average tracking error and mean squared error (MSE) of the thrust force under various given speeds. The definition of MSE is expressed as [27],

$$\text{MSE} = \sqrt{\frac{1}{N} \sum_{i=1}^N (F_e^*(i) - F_e(i))^2} \quad (32)$$

As shown in Fig. 11, both ratios of average error and MSE to the reference are low (<4%), although they increase slightly as the given speed rising. The tracking errors under various conditions verify the good tracking ability of the developed MPTFC method.

B. Dynamic Performance

Secondly, the transient performances under the three control strategies are evaluated. To avoid the mover hitting the end of the machine due to the limited stator distance, the speed reference reverses upon the mover reaches the overtravel-limit switches, which are located at the end of the linear machine.

Fig. 12 illustrates the dynamic performance of speed, phase current, thrust force and stator flux under the speed reversal condition. The references of the thrust force and stator flux (F_e^* and ψ_s^*) are depicted in purple curves and compared with the measured waveforms. As observed, when the speed reverses from -0.6m/s to 0.6m/s, three control methods have similar transient responses to the speed reversal. From the zoomed waveforms in Fig. 12, it can be found that the developed MPTFC has the best thrust force tracking performance during the speed regulation process.

Fig. 13 exhibits the experimental responses of phase current, thrust force, speed and stator flux under load disturbances. The thrust force and speed references have been present in purple curves. When $t=4.05$ s, a sudden load (90N) is applied to the mover, and the total thrust force rises from 220N to 310N. It can be found that the measured speed has a slight fluctuation and then stabilized at the reference (0.6m/s) after 0.15s. Meanwhile, the amplitude of the stator flux also increases slightly, which is in accordance with the simulation in Fig. 7. The experimental results have verified that the developed MPTFC method can offer good dynamic performance at sudden load condition.

TABLE IV
EXPERIMENTAL STEADY-STATE PERFORMANCE UNDER THREE METHODS

Methods	Current THD (%)	Force ripple (%)	Flux ripple (%)
HCC	13.82	8.76	2.46
Conventional MPTFC	9.35	6.82	2.13
Developed MPTFC	4.55	3.56	1.56

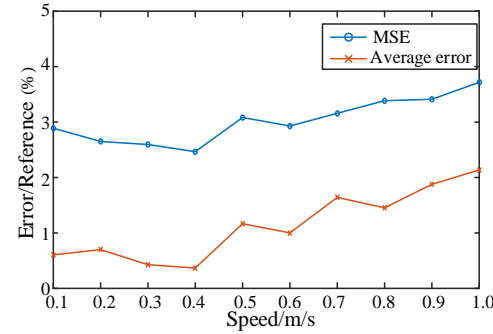


Fig. 11. Tracking errors of thrust force under different speed by the developed MPTFC.

C. Effects of Parameter Variations

Finally, the influences of parameter variations on the performance are experimentally studied. To evaluate the effect of the mover mass on the dynamic speed response, the speed reversal experiment has been conducted with an extra weight of 20kg (40% of the original mover), as shown in Fig. 14. Comparing the speed waveform in Fig. 12(c), the slight speed overshoot can be found with the measured speed waveform in Fig. 14. Additionally, it can be observed that the settling time of the dynamic speed (2s) in Fig. 14 is longer than that (1.3s) in

Fig. 12(c), since the heavier mover will result in a larger inertia and a smaller acceleration when the speed reverses under the same thrust force.

To investigate the effect of parametric variations on the dynamic current response, experimental studies have been conducted under different situations. In the following cases, the speed reference is kept to 0.6m/s. When $t=1$ s, a sudden load (90N) is applied to the mover, and the total thrust force rises from 220N to 310N. Fig. 15 depicts the dynamic responses of the phase current (i_a) and dq -axes currents (i_d/i_q) with the nominal parameters. Then, the phase current and dq -axes current responses under variations of dq -axes inductances (L_d/L_q), phase resistance (R_s) and PM flux-linkage (ψ_f) are shown in Figs. 16-18, respectively. Table V demonstrates THD values of steady-state phase currents under different conditions.

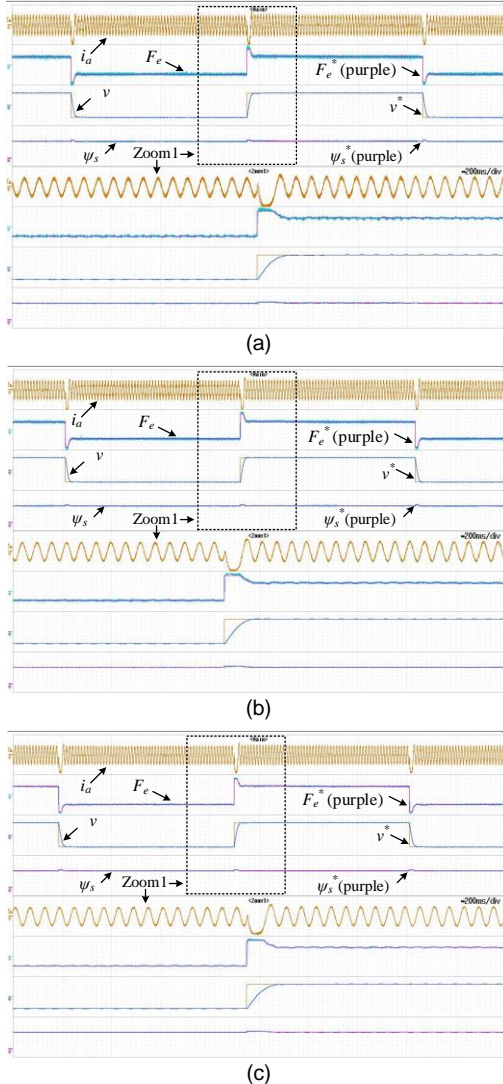


Fig. 12. Measured dynamic waveforms of current, thrust force, speed and stator flux under speed reversal by (a) HCC, (b) conventional MPTFC, (c) the developed MPTFC. (phase current (2A/div), thrust force (100N/div), speed (0.2m/s/div), stator flux (0.05Wb/div), main time (1s/div), zoom1 time (200ms/div))

Firstly, supposing the dq -axes inductances vary by $\pm 50\%$, i.e., $L_d=0.5L_d^*/L_q=0.5L_q^*$, and $L_d=1.5L_d^*/L_q=1.5L_q^*$, respectively, where L_d^* and L_q^* are the nominal values. As can be seen from Fig. 16(a), compared with the case with nominal

dq -axes inductances, higher THD values (8.73% and 6.87%) of the phase current under the load forces of 220N and 310N can be found. However, when the dq -axes inductances increase by 50%, the resultant phase current harmonics change slightly (5.26% and 4.87%) as shown in Fig. 16(b). In addition, it can be observed that the tracking error between the calculated and referenced d -axis current rises when an external load force is added in Fig. 16(b).

In the second case of phase resistance variations, the phase resistance varies also by $\pm 50\%$, i.e., $R_s=0.5R_s^*$, and $R_s=1.5R_s^*$, respectively, where R_s^* is the nominal value. As can be seen from Figs. 17(a) and (b), the variations of phase resistance on the current response are negligible.

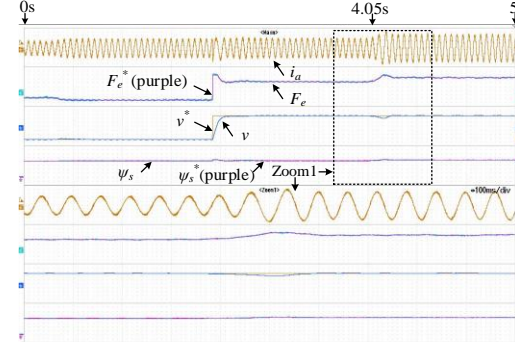


Fig. 13. Measured dynamic waveforms under load disturbance by the developed MPTFC. (phase current (2A/div), thrust force (100N/div), speed (0.2m/s/div), and stator flux (0.05Wb/div). main time (500ms/div), zoom1 time (100ms/div))

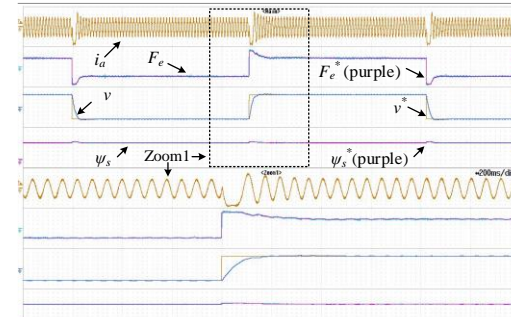


Fig. 14. Measured dynamic waveforms with an extra weight on the mover by the developed MPTFC. (phase current (2A/div), thrust force (100N/div), speed (0.2m/s/div), stator flux (0.05Wb/div), main time (1s/div), zoom1 time (200ms/div))

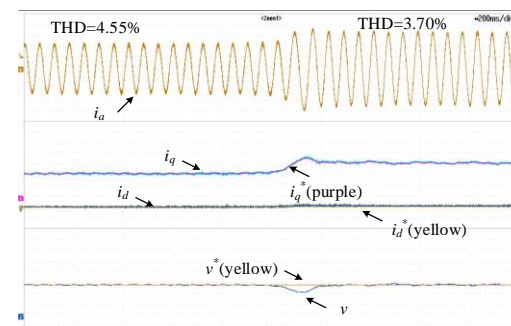


Fig. 15. Measured dynamic current and speed waveforms with nominal parameters by the developed MPTFC. (phase current (2A/div), dq -axes currents (2A/div), speed (0.2m/s/div), time (200ms/div)).

Finally, in term of the PM flux-linkage variations, the phase PM flux-linkage varies by $\pm 20\%$, i.e., $\psi_f=0.8\psi_f^*$ and $\psi_f=1.2\psi_f^*$, respectively, where ψ_f^* is the nominal value. As seen from Fig.

18(a), unfavorable harmonic distortions increase in the phase current waveform (6.57% and 4.83%). And the tracking error of the d -axis current increases as the load force increases under the reduced PM flux-linkage. While when the phase PM flux-linkage increases, the current performance varies slightly as shown in Fig. 18(b).

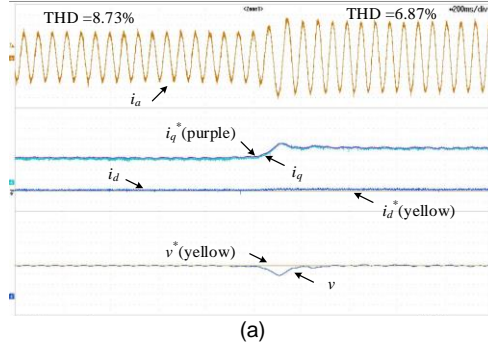


Fig. 16. Measured dynamic current and speed waveforms under inductance variation by the developed MPTFC. (a) $L_d=0.5L_d^*/L_q=0.5L_q^*$. (b) $L_d=1.5L_d^*/L_q=1.5L_q^*$. (phase current (2A/div), dq -axes currents (2A/div), speed (0.2m/s/div), time (200ms/div)).

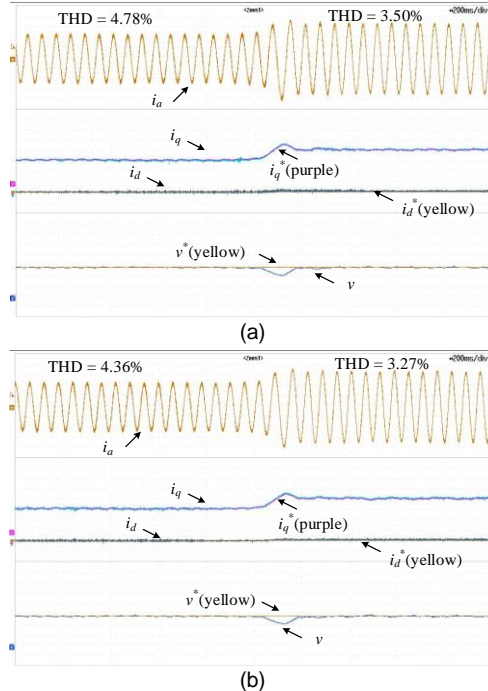


Fig. 17. Measured dynamic current and speed waveforms under resistance variation by the developed MPTFC. (a) $R_s=0.5R_s^*$. (b) $R_s=1.5R_s^*$. (phase current (2A/div), dq -axes currents (2A/div), speed (0.2m/s/div), time (200ms/div)).

Additionally, the transient behaviors of the q -axis current have been also evaluated in terms of the settling time and overshoot, as listed in Table VI. It can be found that overall the three electrical and magnetic parameters uncertainties have slight influences on the dynamic performance of currents. These conclusions agree well with the analysis results in previous studies [28-29].

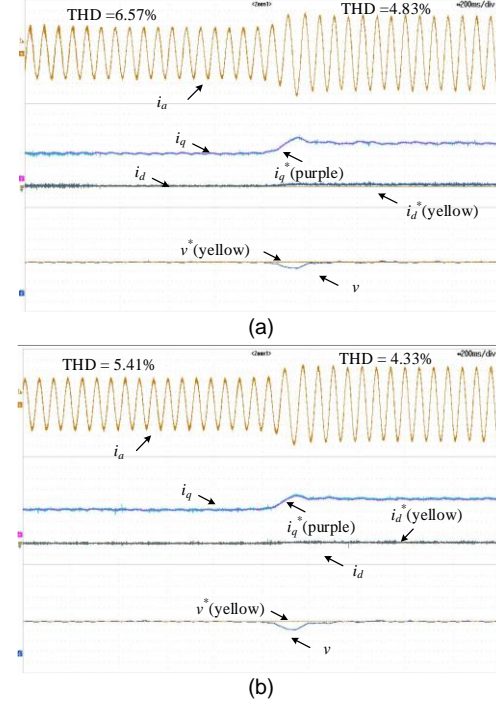


Fig. 18. Measured dynamic current and speed waveforms under PM flux-linkage variation by the developed MPTFC. (a) $\psi_f=0.8\psi_f^*$. (b) $\psi_f=1.2\psi_f^*$. (phase current (2A/div), dq -axes currents (2A/div), speed (0.2m/s/div), time (200ms/div)).

TABLE V
THD VALUES OF STEADY-STATE CURRENT UNDER DIFFERENT CONDITIONS

Conditions	220N	310N
Nominal value	4.55%	3.70%
$L_d=0.5L_d^*/L_q=0.5L_q^*$	8.73%	6.87%
$L_d=1.5L_d^*/L_q=1.5L_q^*$	5.26%	4.87%
$R_s=0.5R_s^*$	4.78%	3.50%
$R_s=1.5R_s^*$	4.36%	3.27%
$\psi_f=0.8\psi_f^*$	6.57%	4.83%
$\psi_f=1.2\psi_f^*$	5.41%	4.33%

TABLE VI
EXPERIMENTAL DYNAMIC CURRENT UNDER DIFFERENT CONDITIONS

Items	Settling time (s)	Overshoot (%)
Nominal value	0.57	16.12
$L_d=0.5L_d^*/L_q=0.5L_q^*$	0.52	19.63
$L_d=1.5L_d^*/L_q=1.5L_q^*$	0.54	17.46
$R_s=0.5R_s^*$	0.55	18.35
$R_s=1.5R_s^*$	0.56	16.87
$\psi_f=0.8\psi_f^*$	0.60	18.75
$\psi_f=1.2\psi_f^*$	0.58	18.04

Apart from speed and current, the thrust force performance under inductance uncertainties in term of the MSE have been also evaluated at the speed of 0.6m/s without external load, as shown in Fig. 19, where ρ means the ratio of the inductance used by the predictive model to the nominal one. It can be observed that both the experiments and simulations indicate

that the similar trends of the thrust force tracking errors in term of MSE due to the inductance variations, which means that both tracking abilities have been affected when the dq -axes inductances vary. It can also be found that the ratio of the MSE to the reference under $\rho < 1$ situation is larger than that under the opposite situation for both experimental and simulation results, and the maximum value is obtained when ρ equals to 0.5.

In summary, the variations of mechanical parameters (the mass of the mover and viscous friction coefficient) can affect the response time of the dynamic speed rather than the tracking ability and steady-state performance. By contrast, the steady-state performance will deteriorate under the variations of inductance and PM flux-linkage.

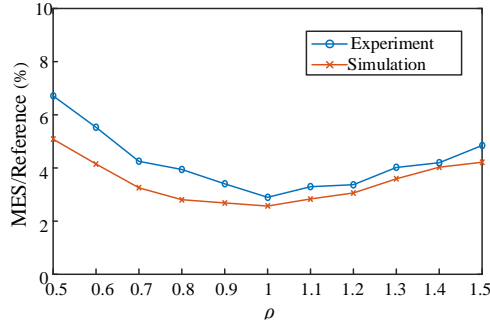


Fig. 19. MSE of thrust force under inductance uncertainties by the developed MPTFC.

VII. CONCLUSION

A MPTFC strategy based on AVVS and TVVS is developed to suppress the thrust force ripple of the CMLFSPM machine. For real-time implementation, the computational burden is reduced by use of the AVVS. The steady-state performance can be improved by using the optimal TVVS. The comparisons among the HCC, the conventional MPTFC and the developed MPTFC show that the developed strategy can decrease the harmonic current as well as ripples of thrust force and stator flux. Besides, the studies of parameter uncertainties demonstrate that the variations of mechanical parameters (the mass of the mover and viscous friction coefficient) mainly affect the transient behaviors, whereas the variations of inductance and PM flux-linkage have more impacts on steady-state performance and tracking ability. The simulated and experimental results of steady-state and dynamic operations are satisfactory and validate the effectiveness of the developed MPTFC method.

REFERENCES

- [1] M. Cheng, W. Hua, J. Zhang and W. Zhao, "Overview of stator-permanent magnet brushless machines," *IEEE Transactions on Industrial Electronics*, vol. 58, no. 11, pp. 5087-5101, Nov. 2011.
- [2] C. F. Wang, J. X. Shen, Y. Wang, L. L. Wang and M. J. Jin, "A new method for reduction of detent force in permanent magnet flux-switching linear motors," *IEEE Transactions on Magnetics*, vol. 45, no. 6, pp. 2843-2846, Jun. 2009.
- [3] R. Cao, M. Cheng, W. Hua, W. Zhao and Y. Du, "A new primary permanent magnet linear motor for urban rail transit," *2010 International Conference on Electrical Machines and Systems*, Incheon, 2010, pp. 1528-1532.
- [4] R. Cao, M. Cheng, C. Mi, W. Hua, X. Wang and W. Zhao, "Modeling of a complementary and modular linear flux-switching permanent magnet motor for urban rail transit applications," *IEEE Transactions on Energy Conversion*, vol. 27, no. 2, pp. 489-497, Jun. 2012.
- [5] R. Cao, M. Cheng and W. Hua, "Investigation and general design principle of a new series of complementary and modular linear FSPM motors," *IEEE Transactions on Industrial Electronics*, vol. 60, no. 12, pp. 5436-5446, Dec. 2013.
- [6] R. Cao, M. Cheng and B. Zhang, "Speed control of complementary and modular linear flux-switching permanent-magnet motor," *IEEE Transactions on Industrial Electronics*, vol. 62, no. 7, pp. 4056-4064, July 2015.
- [7] M. Cheng, F. Yu, K. T. Chau and W. Hua, "Dynamic performance evaluation of a nine-phase flux-switching permanent-magnet motor drive with model predictive control," *IEEE Transactions on Industrial Electronics*, vol. 63, no. 7, pp. 4539-4549, Jul. 2016.
- [8] W. Huang, W. Hua, F. Yu, "A model predictive current control of flux-switching permanent magnet machines for torque ripple minimization", *AIP Advances*, vol. 7, no. 5, pp. 056609, May. 2017.
- [9] W. Xu, "Novel decoupling model-based predictive current control strategy for flux-switching permanent-magnet synchronous machines with low torque ripple and switching loss," *IEEE Transactions on Applied Superconductivity*, vol. 24, no. 5, pp. 1-5, Oct. 2014.
- [10] Gregor, R., Barrero, F., Toral, S.L., et al., "Predictive-space vector PWM current control method for asymmetrical dual three-phase induction motor drives," *IET Electric Power Applications*, vol. 4, no. 1, pp. 26-34, Jan. 2010.
- [11] S. Vazquez, J. Rodriguez, M. Rivera, L. G. Franquelo and M. Norambuena, "Model predictive control for power converters and drives: advances and trends," *IEEE Transactions on Industrial Electronics*, vol. 64, no. 2, pp. 935-947, Feb. 2017.
- [12] F. Wang, S. Li, X. Mei, W. Xie, J. Rodríguez and R. M. Kennel, "Model-based predictive direct control strategies for electrical drives: an experimental evaluation of PTC and PCC methods," *IEEE Transactions on Industrial Informatics*, vol. 11, no. 3, pp. 671-681, Jun. 2015.
- [13] Rodriguez, J., Kennel, R.M., Espinoza, J.R., et al., "High-performance control strategies for electrical drives: an experimental assessment," *IEEE Transactions on Industrial Electronics*, vol. 59, no. 2, pp. 812-820, Feb. 2012.
- [14] W. Hua, W. Huang and F. Yu, "Improved model-predictive-flux-control strategy for three-phase four-switch inverter-fed flux-reversal permanent magnet machine drives," *IET Electric Power Applications*, vol. 11, no. 5, pp. 717-728, May. 2017.
- [15] Y. Zhang, and H. Yang, "Model predictive torque control of induction motor drives with optimal duty cycle control," *IEEE Transactions on Power Electronics*, vol. 29, no. 12, pp. 6593-6603, Dec. 2014.
- [16] M. H. Vafaie, B. Mirzaei Dehkordi, P. Moallem and A. Kiyomarsi, "Minimizing torque and flux ripples and improving dynamic response of PMSM using a voltage vector with optimal parameters," *IEEE Transactions on Industrial Electronics*, vol. 63, no. 6, pp. 3876-3888, Jun. 2016.
- [17] Y. Zhang and H. Yang, "Generalized two-vector-based model-predictive torque control of induction motor drives," *IEEE Transactions on Power Electronics*, vol. 30, no. 7, pp. 3818-3829, Jul. 2015.
- [18] Y. Zhang and H. Yang, "Two-vector-based model predictive torque control without weighting factors for induction motor drives," *IEEE Transactions on Power Electronics*, vol. 31, no. 2, pp. 1381-1390, Feb. 2016.
- [19] M. R. Nikzad, B. Asaei, and S. O. Ahmadi. "Discrete duty-cycle-control method for direct torque control of induction motor drives with model predictive solution," *IEEE Transactions on Power Electronics*, vol. 33, no. 3, pp. 2317-2329, Mar. 2018.
- [20] W. Xie, X. Wang, F. Wang, W. X., et al., "Finite-control-set model predictive torque control with a deadbeat solution for PMSM drives," *IEEE Transactions on Industrial Electronics*, vol. 62, no. 9, pp. 5402-5410, Sep. 2015.
- [21] Y. Zhang and J. Zhu, "A novel duty cycle control strategy to reduce both torque and flux ripples for DTC of permanent magnet synchronous motor drives with switching frequency reduction," *IEEE Transactions on Power Electronics*, vol. 26, no. 10, pp. 3055-3067, Oct. 2011.
- [22] M. A. M. Cheema, J. E. Fletcher, D. Xiao and M. F. Rahman, "A direct thrust control scheme for linear permanent magnet synchronous motor based on online duty ratio control," *IEEE Transactions on Power Electronics*, vol. 31, no. 6, pp. 4416-4428, Jun. 2016.
- [23] G. S. Buja and M. P. Kazmierkowski, "Direct torque control of PWM inverter-fed AC motors - a survey," *IEEE Transactions on Industrial Electronics*, vol. 51, no. 4, pp. 744-757, Aug. 2004.

- [24] T. J. Liang and K. C. Tseng, "Analysis of integrated boost-flyback step-up converter," *IEE Proceedings - Electric Power Applications*, vol. 152, no. 2, pp. 217-225, 4 March 2005.
- [25] dSPACE DS1104 Manual, Paderborn, Germany, dSPACE Inc., 2004.
- [26] P. Cortes, J. Rodriguez, C. Silva and A. Flores, "Delay compensation in model predictive current control of a three-phase inverter," *IEEE Transactions on Industrial Electronics*, vol. 59, no. 2, pp. 1323-1325, Feb. 2012.
- [27] B. Bogado, F. Barrero, M. R. Arahal, S. Toral and E. Levi, "Sensitivity to electrical parameter variations of Predictive Current Control in multiphase drives," *IECON 2013 - 39th Annual Conference of the IEEE Industrial Electronics Society*, Vienna, 2013, pp. 5215-5220.
- [28] J. Rodriguez and P. Cortes, *Predictive control of power converters and electrical drives*. New York, NY, USA: Wiley, 2012.
- [29] H. A. Young, M. A. Perez and J. Rodriguez, "Analysis of Finite-Control-Set Model Predictive Current Control with Model Parameter Mismatch in a Three-Phase Inverter", *IEEE Transactions on Industrial Electronics*, vol. 63, no. 5, pp. 3100-3107, May 2016.



Wentao Huang received the B.Sc. degree in automation from the School of Information Science and Engineering, Ningbo Institute of Technology, Zhejiang University, Ningbo, China, in 2012, and M.Sc. degree in control theory and control engineering from the School of Electrical and Information Engineering, Jiangsu University, Zhenjiang, China, in 2015. Since 2015, he has been working toward the Ph.D. degree in the School of Electrical Engineering, Southeast University, China. He is currently a joint Ph.D. student with the School of Electrical and Data Engineering, University of Technology Sydney, NSW, Australia. His major research interests include permanent magnet machine drives and model predictive control.



Wei Hua (M'03-SM'16) received B.Sc. and Ph.D. degrees both in Electrical Engineering from the School of Electrical Engineering, Southeast University, Nanjing, China, in 2001 and 2007, respectively. During 2004.9-2005.8, he visited the department of Electronics and Electrical Engineering, The University of Sheffield, UK, as a joint-supervised Ph. D student. Since 2007, he has been with Southeast University, where he is currently a Professor with the School of Electrical Engineering. He is the author or coauthor of over 150 technical papers, and he is the holder of 50 patents in his areas of interest. His teaching and research interests include the design, analysis, and control of electrical machines.



Fangbo Yin received the B.Eng. degree in automation from the College of Automation Engineering, Nanjing University of Posts and Telecommunications, Nanjing, China, in 2013. He is currently working toward the M.Eng. degree in electrical engineering at the School of Electrical Engineering, Southeast University, Nanjing. His research interests include the drive and control of permanent magnet machines.



Feng Yu (M'17) received the B.Eng. degree from the School of Electrical Engineering, Sanjiang University, Nanjing, China, in 2008, the M.Sc. degree from the School of Electrical and Information Engineering, Jiangsu University, Zhenjiang, China, in 2011, and the Ph.D. degree in the School of Electrical Engineering, Southeast University, Nanjing, China, in 2016.

Since 2016, he has been with Nantong University, Nantong, China, where he is currently an Assistant Professor in the School of Electrical Engineering. His current research interests include the control of multiphase machines and drives for applications ranging from automotive to renewable energy.



Ji Qi received the B.Sc. degree from the School of Electrical Engineering, Southeast University, Nanjing, China, in 2016. He is currently working toward the M.Sc. degree in electrical engineering at Southeast University, Nanjing, China. His current research interests include design and control of stator-excited brushless machines.